Mixing rates and vertical heat fluxes north of Svalbard from Arctic winter to spring

Amelie Meyer[1], Ilker Fer[2], Arild Sundfjord[1], and Algot K. Peterson[2]

Key words: Mixing, heat flux, Arctic, Yermak Plateau, sea ice melt, Atlantic Water inflow, microstructure profiler, storms, upper ocean, N-ICE2015, turbulence.

Key points:

- Storms above Atlantic Water induce rapid basal melt events of 25 cm/day and 100 $\mathrm{W\,m^{-2}}$ average ocean heat fluxes at the ice-ocean interface
- Nansen Basin winter mean heat flux across the pycnocline is 3 $\mathrm{W\,m^{-2}}$ in calm conditions and grows significantly to 5 $\mathrm{W\,m^{-2}}$ when including storms
- Ratio of relative effect on heat fluxes of storms over Atlantic Water to Atlantic Water only to storms to calm deep basin is $6 : 5 : 2 : 1$

Corresponding author: A. Meyer, Norwegian Polar Institute, Fram Centre, 9296 Tromsø, Norway. (Amelie.Meyer@npolar.no)

[1]Norwegian Polar Institute, Fram Centre,
9296 Tromsø, Norway.

[2]Geophysical Institute, University of
Bergen and Bjerknes Centre for Climate
Research, Bergen, Norway.

Abstract. Mixing and heat flux rates collected in the Eurasian Basin north of Svalbard during the N-ICE2015 drift expedition are presented. The observations cover the deep Nansen Basin, the Svalbard continental slope and the shallow Yermak Plateau from winter to summer. Mean quiescent winter heat flux values in the Nansen Basin are $2\,\mathrm{W\,m^{-2}}$ at the ice-ocean interface, $3\,\mathrm{W\,m^{-2}}$ in the pycnocline and $1\,\mathrm{W\,m^{-2}}$ below the pycnocline. Large heat fluxes exceeding $300\,\mathrm{W\,m^{-2}}$ are observed in the late spring close to the surface over the Yermak Plateau. The data consisting of 588 microstructure profiles and 50 days of high-resolution under-ice turbulence measurements are used to quantify the impact of several forcing factors on turbulent dissipation and heat flux rates. Wind forcing increases turbulent dissipation seven times in the upper 50 m, and doubles heat fluxes at the ice-ocean interface. Presence of warm Atlantic Water close to the surface increases the temperature gradient in the water column, leading to enhanced heat flux rates within the pycnocline. Steep topography consistently enhances dissipation rates by a factor of four and episodically increases heat flux at depth. It is, however, the combination of storms and shallow Atlantic Water that leads to the highest heat flux rates observed: Ice-ocean interface heat fluxes average $100\,\mathrm{W\,m^{-2}}$ during peak events and are associated with rapid basal sea ice melt, reaching $25\,\mathrm{cm\,day^{-1}}$.

1. Introduction

Energy from winds, ocean tides, and currents fuels turbulence in the oceans, leading to highly variable and intermittent mixing of tracers and momentum in the water column. Magnitude, spatial distribution, and temporal evolution of ocean mixing affect watermass transformations, large scale ocean circulation, and in polar regions, the extent and variability of sea ice cover. Interior mixing is primarily attributed to the breaking of internal waves, generated by wind forcing at the ocean surface and by the interaction of tides and currents with topographic features on the sea floor. In the Arctic, the sea ice at the surface reduces the transfer of wind energy to the ocean [*Morison et al.*, 1985; *Pinkel*, 2005], and observed turbulent dissipation rates are an order of magnitude smaller than at lower latitudes [*Fer*, 2009]. Mixing rates in the Arctic water column away from the boundaries are therefore typically dominated by small double diffusive fluxes and lateral intrusions [*Lenn et al.*, 2009; *Sirevaag and Fer*, 2012; *Guthrie et al.*, 2013].

Nevertheless, areas with enhanced mixing rates have been identified in recent years [*Rainville and Winsor*, 2008; *Shaw and Stanton*, 2014; *Rippeth et al.*, 2015], such as the Yermak Plateau north of Svalbard [*Padman and Dillon*, 1991; *Steele and Morison*, 1993; *Sirevaag and Fer*, 2009]. Mixing in these hotspots is linked to rough topography and strong barotropic tides [*Padman and Dillon*, 1991; *Fer et al.*, 2010]. At the latitude of the Yermak Plateau, the energy extracted from the semidiurnal barotropic tide cannot propagate away as linear internal waves and dissipates locally, where the internal tide is forced [*Fer et al.*, 2015]. The large dissipation rates near the Yermak Plateau have

potential to modify water masses flowing into the Arctic and impact ice cover in the region [*Untersteiner*, 1988; *Carmack et al.*, 2015].

The Atlantic Water inflow is the main source of oceanic heat to the Arctic Ocean. With ocean surface heat fluxes above the path of Atlantic Water inflow that can reach $100\,\mathrm{W\,m^{-2}}$ near Svalbard [*Aagaard et al.*, 1987; *Dewey et al.*, 1999; *Sirevaag and Fer*, 2009], this warm inflow has the capacity to melt Arctic sea ice in the area. Downstream of Fram Strait, however, the heat carried by Atlantic Water is isolated from the sea ice by stratification in the form of a cold layer of Polar Surface Water. A mean Arctic Ocean surface heat flux of $2\,\mathrm{W\,m^{-2}}$ has been estimated the necessary flux to keep the sea ice thickness at equilibrium [*Maykut and McPhee*, 1995]. Observations have indicated mean surface heat fluxes of $3.5\,\mathrm{Wm^2}$ Arctic wide [*Krishfield and Perovich*, 2005].

A key question in polar oceanography is on the role of oceanic heat fluxes in the energy budget and mass balance of the new thinner Arctic sea ice [*Polyakov et al.*, 2013; *Carmack et al.*, 2015]. How much heat from Atlantic Water reaches the sea ice and what drives the heat flux? The Norwegian young sea ICE expedition (N-ICE2015) took place north of Svalbard in 2015 to investigate the new thinner Arctic sea ice regime [*Renner et al.*, 2014] and associated interactions between the ice, ocean, and atmosphere, and the feedback between physical and biogeochemical processes [*Granskog et al.*, 2016].

We present mixing and heat flux observations collected from January to June 2015 during N-ICE2015 in the Nansen Basin and over the Yermak Plateau. We investigate the turbulence and heat flux climate, focusing on sources of forcing. The campaign, data set, and methods are described in section 2. In section 3, we give a brief overview of the regional oceanography. Mixing and heat flux estimates are presented in section 4. Sources

of forcing and impact on the sea ice are discussed and conclusions summarized in section 5.

2. Data and methods

2.1. N-ICE2015 campaign

Between January and June 2015, the Research Vessel (RV) Lance completed four drifts in the Arctic north of Svalbard anchored each time to a different sea ice floe (Fig. 1 and Table 1). On each floe, hereinafter referred to as Floe 1 to Floe 4, an ice camp was set up and oceanographic data as well as atmospheric, sea ice, snow, and biogeochemical data were collected [*Granskog et al.*, 2016].

Floe 1 took place in January and February 2015 lasting 38 days, partly in the Nansen Basin, partly at the northern edge of the Yermak Plateau, finishing on the Svalbard continental slope (Table 1). Floe 2 lasted 24 days over the Nansen Basin during February and March 2015. Floe 3, the longest, lasted 49 days from April until June 2015 from the northern slope of the Yermak Plateau, to the southern edge of the Plateau. Finally Floe 4 was 16 days long and covered a track parallel to the last part of Floe 3 on the Yermak Plateau. We define data from January, February and March as winter data (Floe 1 and Floe 2). Data from April, May and June are spring data (Floe 3 and Floe 4), which we further split into early spring, prior to 25 May and late spring after 25 May 2015.

2.2. Microstructure profiler data

During the N-ICE2015 campaign, a total of 588 microstructure profiles were collected in 173 sets with two loosely tethered free-fall MSS-90 microstructure profilers [*Prandke and Stips*, 1998] developed by ISW Wassermesstechnik. A set, which corresponds to

consecutively sampled profiles, was usually composed of three profiles. It took between 10 and 20 minutes to record each profile depending on drift conditions. Most days, three sets of profiles were spread between 8 am and 8 pm (UTC). Bad weather occasionally restricted access to the sampling site resulting in several days without microstructure profiles. Throughout the six months, frequency of microstructure sampling increased with improving working conditions as the air temperature rose from as low as $-40\,°\mathrm{C}$ in winter to $0\,°\mathrm{C}$ in late spring (after 25 May).

The profilers had precision conductivity, temperature, and pressure sensors as well as microstructure sensors including two airfoil shear probes, a fast response thermistor, and a micro conductivity sensor, all sampling at 1024 Hz. The profiler was deployed through a hole in the ice from a heated tent, several hundred meters away from the ship. The profiles (only the downcasts are used) started immediately below the ice and reached on average 150 m during Floe 1 and 300 m during Floe 2, 3, and 4. Data processing followed *Fer* [2006, 2014]. Final processed profiles include 0.2 m vertically averaged temperature and salinity, and 1 m vertically averaged turbulent dissipation rate (Section 2.3). Reported accuracies of the sensors by the manufacturer were 0.1 m, $0.002\,°\mathrm{C}$, and $0.003\,\mathrm{ms\,cm^{-1}}$ for pressure, temperature, and conductivity respectively.

The Conductivity Temperature and Depth (CTD) data from the microstructure profilers were compared with the ship CTD data for validation, and salinity drift corrections of $0.021\,\mathrm{g\,kg^{-1}}$ for one and $0.065\,\mathrm{g\,kg^{-1}}$ for the other profiler were applied. A detailed description of the ship CTD data from the N-ICE2015 expedition is given in *Meyer et al.* [2017]. The data were analyzed using the Thermodynamic Equation of SeaWater 2010 (TEOS-

10) and Conservative Temperature (Θ) and Absolute Salinity (S_A) are used throughout the text [*McDougall et al.*, 2012].

2.3. Estimating dissipation and heat flux from microstructure profiler data

Assuming local small-scale isotropy [*Yamazaki and Lueck*, 1990] and using shear data, profiles of the dissipation rate of turbulent kinetic energy were derived, hereinafter referred to as dissipation rate, ϵ ($\mathrm{W\,kg^{-1}}$)

$$\epsilon = 7.5\nu\langle u_z'^2\rangle, \tag{1}$$

where ν is the molecular viscosity of seawater, $\langle u_z'^2\rangle$ is the shear variance of horizontal small scale velocity and brackets indicate averaging. The shear variance was obtained from integrating the wave number spectrum from 1 s long segments. The lowest detection level of the dissipation rate was $(1-3)\times 10^{-9}$ $\mathrm{W\,kg^{-1}}$. The dissipation rate profiles were vertically averaged in 1 m bins.

The diapycnal turbulent eddy diffusivity of mass, hereinafter referred to as diffusivity (K_ρ), was calculated from the dissipation rate (ϵ), using the *Osborn* [1980] relation

$$K_\rho = \Gamma\frac{\epsilon}{N^2}. \tag{2}$$

Here Γ, a factor related to the mixing efficiency, is set to 0.2, the standard value in the literature, and N is the buoyancy frequency averaged over 4 m bins. The turbulent heat flux F_H ($\mathrm{W\,m^{-2}}$) is then calculated as

$$F_H = -\rho_0 C_p K_\rho \frac{d\Theta}{dz}, \tag{3}$$

where $\rho_0 = 1027\ \mathrm{kg\,m^{-3}}$ is the seawater density, and $C_p \approx 3991.9\ \mathrm{J\,kg^{-1}\,K^{-1}}$ is the specific heat of seawater [*Intergovernmental Oceanographic Commission*, 2010]. In the calculations of K_ρ and $d\Theta/dz$, vertical gradients are taken over 1-m vertical scale and the profiles are averaged over 4 m bins. The sign convention is that positive heat fluxes correspond to upward heat fluxes in the water column.

With the caveat of a constant mixing efficiency assumption, the microstructure profiler allows us to measure the turbulent heat flux in the upper 300 m of the water column. When stratification is close to noise level however, measurements suffer from uncertainty in diffusivity, a direct consequence of the idealized kinetic energy budget of the stratified turbulence employed in the Osborn model. To remove unreliable heat flux estimates, segments of buoyancy frequency that were below noise level ($3 \times 10^{-6}\ \mathrm{s^{-2}}$) were set to noise level, and those with temperature gradient magnitude below noise level ($5 \times 10^{-4}\ ^\circ\mathrm{C\,m^{-1}}$) were set to zero. Measurements of the dissipation rate are not affected by weak stratification, and are reliable throughout the water column, except in the upper 3-4 m, where the profiler adjusts to free fall.

2.4. Turbulence instrument cluster data

High-resolution turbulence measurements were made in the ice-ocean boundary layer using Turbulence Instrument Clusters (TICs) deployed through a hole at 1 m below the ice undersurface. Currents were measured by a Sontek acoustic Doppler velocimeter (ADV), sampling a $2\,\mathrm{cm}^3$ volume with a 24 Hz sampling rate, averaged to 2 Hz. Temperature and conductivity were measured using SeaBird sensors, with a sampling rate of 24 Hz, averaged to 3 Hz. Time series measurements of 3-D velocity components and temperature were thus collected resolving the energy spectrum from energy containing eddies through

to the inertial subrange of turbulence. A detailed description of the set-up is given by *Peterson et al.* [2017].

Calculations were based on 15-minute segments over which the current components were rotated into the mean current direction. The data set was also systematically quality controlled to exclude any segment with a low signal-to-noise ratio, non-stationarity, or other contamination, before calculating turbulent momentum and heat fluxes. Friction velocity was calculated from velocity covariances, to a noise level of $0.2\,\mathrm{cm\ s^{-1}}$. Temperature measurements in the same measurement volume were used to calculate the vertical heat flux at 1 m below the ice with $0.1\,\mathrm{W\ m^{-2}}$ noise level. A complete description of the quality control process and calculations is given in *Peterson et al.* [2017]. Out of 74 day long TIC data, a total length of 50 days passed the quality control. Throughout the text, mixing and heat flux estimates at the ice-ocean interface are from Turbulence Instrument Cluster (TIC) data, while all other estimates are from microstructure profiler data. For both the TIC and the microstructure profiler data, the ice-ocean interface refers to measurements at 1 m below the ice.

2.5. Other data sets

Auxiliary data include navigation data from the vessel to estimate drift speed; bathymetry data from the International Bathymetric Chart of the Arctic Ocean (IBCAO version 3.0) to derive topographic slope [*Jakobsson et al.*, 2012]; atmospheric storms characteristics described in *Cohen et al.*; ice thickness measurements from Ice Mass Balance (IMB) buoys described in *Provost et al.* [2017] and *Itkin et al.* [2015]; and distance to open water from *Itkin et al.*.

Atmospheric measurements were made both from the ship and on the ice floes. Near-surface meteorological parameters were collected on a 10 m high tower on the ice, 300 to 400 meters away from the ship to minimize interference from the ship. Temperature, humidity, and wind sensors were mounted on the tower approximately 2, 4 and 10 m above the snow surface [*Cohen et al.*]. Ship-based measurements of temperature, pressure, and wind provided data to fill some gaps in the tower data. The ship-based instruments were mounted on the ship's mast approximately 22-24 m above the ice surface. Instrumentation details are given in *Cohen et al.*, Table 1.

IMB buoys have thermistor chains that measure the temperature and a resistivity proxy along a 5 m cable that goes through the air, the snow, the ice and the ocean below the ice. From these data, the interfaces between each medium was identified and the thickness of the snow and ice layers were estimated with a 2 cm vertical resolution [*Rösel et al.*, 2016] for Floe 1, Floe 2 and Floe 3. There was no ice mass balance buoy data available for Floe 4. The definitions of the interfaces were based on the temperature profiles and the thermal resistivity proxy described by *Provost et al.* [2017]. Ice types and characteristics for each floe are described in *Rösel et al.* [2016].

Distance to open water was estimated as the shortest distance from R.V. Lance to the inner edge of the ice class 'open water' ($< 10\%$) based on navigational sea ice charts produced by the Norwegian Meteorological Institute from satellite data [*Itkin et al.*].

2.6. Defining oceanographic parameters

2.6.1. The 0 °C isotherm

We defined the boundary between waters from the Arctic at the surface and waters with Atlantic origin at intermediate depths (either Modified Atlantic Water or Atlantic Water)

as the 0 °C isotherm. During the N-ICE2015 campaign, the 0 °C isotherm was found at approximately 100 m depth from January until May and between 25 m and 75 m depth in June (Fig. 2b, white line).

2.6.2. Atlantic Water

Atlantic Water was defined in terms of density and temperature as follow: $27.70 < \sigma_0 < 27.97$ and $\Theta > 2^oC$ [*Rudels et al.*, 2000]. The depth of the upper boundary of Atlantic Water, different from the depth of the 0 °C isotherm, was found as shallow as 30 m depth and as deep as 300 m.

2.6.3. Mixed layer depth

The microstructure profiler temperature and salinity data averaged in 1 m bins were used to derive the depth of the mixed layer (Fig. 2c, black line). In winter, the mixed layer depth was defined as the depth in each profile where the potential density first exceeded the density at 20 m depth by $0.01\,\mathrm{kg\,m^{-3}}$. In spring we found the depth in each profile where the potential density first exceeded the near-surface value by $0.003\,\mathrm{kg\,m^{-3}}$ (usually at 2 m depth). The lower density criterion used for spring was chosen to avoid identifying deeper stratification steps, such as remnants of winter mixed layer, as the mixed layer depth. Overall, the mixed layer depth estimates were not very sensitive to the choice of density criteria. These criteria definitions are typical for the Arctic region [*Peralta-Ferriz and Woodgate*, 2015].

2.6.4. Pycnocline depth and layer

The pycnocline depth was identified as the depth of maximum N^2 using the 4 m smoothed N^2 profiles (Fig. 2b and c, red line). The pycnocline layer over which variables were averaged was based on the distance (dz) between the mixed layer depth and

the pycnocline depth, with the mixed layer typically shallower than the pycnocline: the pycnocline layer was defined as $2 \times dz$ and centred on the pycnocline depth. When there was no mixed layer, dz was set to 2 m; when the mixed layer and pycnocline had the same depth, dz was set to 1 m; and when the pycnocline depth was less than 3 m, we defined no pycnocline layer. The base of the pycnocline was defined as the bottom of the pycnocline layer.

2.6.5. Bulk calculations

Further in the text, bulk values of heat fluxes, buoyancy frequencies, and temperature gradients are discussed for the mixed layer, the pycnocline layer, and for the layer below the pycnocline (from 30 m below the pycnocline depth to the deepest data point). For each set-averaged profile, the bulk estimates of heat flux in a layer refer to a heat flux that was derived using Eq. 3 where diffusivity is a bulk value for that layer (from the layer-averaged dissipation rate and buoyancy frequency for that set) and where the temperature gradient ($d\Theta/dz$) is a bulk estimate for that layer.

2.7. Defining forcing conditions

Various forcing and environmental conditions were analysed to put the dissipation rate and heat flux estimates in perspective. We considered both winds and topography as direct forcing mechanisms that would influence mixing and heat flux intensity. We also considered the presence of Atlantic Water at depth as an indirect forcing mechanism that could increase the temperature gradient in the water column below the ice.

2.7.1. Wind

Wind forcing events were identified using the storm classification developed for N-ICE2015 data set presented in *Cohen et al.*. In those definitions, storms covered periods

when 10 minute averaged wind speeds were continuously greater than $8\,\mathrm{m\,s^{-1}}$ for at least 1 hour. Altogether, 18 storms that are indicated along the drift tracks in Fig. 1, took place during the expedition, labelled either 'major' (M1 through M8) or 'minor' (m1 through m10, see Table 2 in *Cohen et al.*). We then further identified storms that were key in terms of oceanic response: these six key storms are the subset of storms associated with sea ice drift speeds larger than $0.4\,\mathrm{m\,s^{-1}}$, a combination of both major and minor storms: storm M2, M3, M7, m7, M8 and m10.

Periods of the N-ICE2015 drifts when storms took place, including key storms, and when there were no steep topography and no Atlantic Water in the water column, were labelled 'storms only' periods. Periods when key storms took place and when there were no steep topography and no Atlantic Water in the water column, were labelled 'key storms only' periods.

2.7.2. Topography

The interaction of currents (tidal and geostrophic) with topographical features can result in disturbances in the stratified water, which can lead to enhanced mixing locally or away from the generation site. Here we used the steepness of topography to identify where topography could be affecting mixing and heat fluxes. Steep topography was defined when slope angles are larger than the 90th percentile ($2.6\,^{\circ}$) and flat topography when slope angles were less than the 10th percentile ($0.057\,^{\circ}$), where the slopes angle for each microstructure set and each point of the drift track were computed over a $0.2\,^{\circ}$ longitude by $0.2\,^{\circ}$ latitude box using the IBCAO version 3.0 topography data set [*Jakobsson et al.*, 2012]. We also ran the analysis using the roughness of topography rather than the steepness, as done in similar works [*Meyer et al.*, 2015], giving similar results (not shown).

The microstructure sets were not sampled continuously throughout the N-ICE2015 expedition and as a result, sections of the drift tracks that are labelled steep or flat (Fig. 2c red or yellow blocks) do not always contain microstructure sets. This is the case in particular for the end of Floe 3 over steep patches of topography, when none of the collected microstructure sets for that period qualify as over steep topography (Fig. 2c red, yellow and black triangles).

Data from the N-ICE2015 drifts when there was steep topography, but no storms and no Atlantic Water in the water column were labelled 'topography only' data. Data from the N-ICE2015 drifts when there was flat topography, no storms, and no Atlantic Water in the water column were labelled 'flat topography only' data.

2.7.3. Atlantic Water presence

The presence of Atlantic Water, an indirect forcing mechanism, was defined as when the distance between the upper limit of Atlantic Water and pycnocline depth was less than 100 m (Fig. 2b, red diamonds).

Data from the N-ICE2015 drifts when the distance between the upper limit of Atlantic Water and pycnocline depth was less than 100 m, when there were no storms, and no steep topography, were labelled 'Atlantic Water only' data.

2.7.4. No forcing

Data from the N-ICE2015 drifts when no storm took place, topography was not steep, and when Atlantic Water was not present in the water column, were labelled 'no forcing' data. In these 'no forcing' data, the key forcing mechanisms listed above were not involved; it does not, however, exclude the presence of other forcing mechanisms not discussed here.

3. Background: Regional oceanography

The hydrographic conditions, mixed layer properties, and currents characteristics during the N-ICE2015 campaign are described in detail in *Meyer et al.* [2017]. This section provides a short summary. In winter (January, February and March) and early spring (April and May), the upper 50 m were close to freezing point, while in late May and June, inflowing Atlantic Water with temperatures above 2 °C was encountered 50-100 m below the sea ice (Fig. 3a, red profile). After 25 May 2015, when Atlantic Water was shallow and close to the sea ice, salinity decreased in the upper 25 m and stratification increased dramatically (Fig. 3b and c, red profiles).

3.1. Water masses

During the drifts, six different water masses were identified using the *Rudels et al.* [2000] classification. At the surface, we found a layer of Polar Surface Water ($\sigma_0 < 27.70$ and $\theta < 0^oC$) throughout the N-ICE2015 expedition, on average 93 m thick in winter and 78 m thick in spring. Patches of warm Polar Surface Water ($\sigma_0 < 27.70$ and $\theta > 0^oC$), a signature of ice melt water, were observed in the upper 50 m during spring on the Yermak Plateau, at the end of Floe 3 and 4. Atlantic Water ($27.70 < \sigma_0 < 27.97$ and $\theta > 2^oC$) was observed both on the continental slope of Svalbard and on the Yermak Plateau. On the Yermak Plateau, Atlantic Water was found between 100 m and 500 m depth. Atlantic Water mean temperature was 2.7 °C and mean salinity 35.15 g kg^{-1}, with a maximum temperature of 4.4 °C. Modified Atlantic Water ($27.70 < \sigma_0 < 27.97$ and $\theta < 2^oC$) is the result of Atlantic Water cooling and mixing with polar waters as it circulates through the Arctic. It was found from approximately at 100 m to 500 m depth unless Atlantic Water

was present. Intermediate Water ($27.97 < \sigma_0$, $\sigma_{0.5} < 30.444$ and $\theta < 0^oC$) and Nordic Deep Water ($\sigma_{0.5} > 30.444$) were found from 900 m and below [*Meyer et al.*, 2017].

3.2. Atlantic Water inflow

The Atlantic Water inflow was observed partly flowing along the Svalbard coast (Svalbard Branch) at the end of Floe 1, and partly flowing around the Yermak Plateau (Yermak Branch). Its presence on the Yermak Plateau was associated with a shallow mixed layer and low sea ice cover. On the western side of the Yermak Plateau, Atlantic Water observed from 130 m depth with 2.8 degreeCelsius mean temperature was identified as part of the Yermak Branch of inflowing Atlantic Water. At the northern end of the Yermak Plateau, the Yermak Branch was observed retroflecting around the northern tip of the Plateau, at 130 m depth, with 2.1 °C mean temperature above the 1500 m isobaths. Further downstream, along the eastern side of the Yermak Plateau, the Yermak Branch was seen cooler, eroding after circulating around the Yermak Plateau. Winter hydrography discussed more in detail in *Koenig et al.* [2016] showed three Atlantic Water pathways across and around the Yermak Plateau. Finally, the Svalbard branch of inflowing Atlantic Water was clearly observed in the ocean current observations between the 600 and 1000 m isobaths at 81.5 °N in February [*Meyer et al.*, 2017].

3.3. Mixed layer characteristics

The mean mixed layer depth for the expedition was 44 m. The deepest mixed layers were observed in March and the shallowest in June. In winter, the mixed layer was close to freezing with the departure from freezing temperature in the mixed layer δT=0.03 °C. Using an idealized 1-D model, *Fer et al.* [2017] reproduced the observed evolution of the

mixed layer hydrography in winter, suggesting that vertical processes dominated. They report only 10% increase in salinity as a result of freezing and brine release, significantly less than that due to entrainment (90%) from beneath the mixed layer. During Floe 3, δT doubled to 0.06 °C and it reached very large values in June with a mean of 0.47 °C during Floe 4. A dramatic change was seen in mixed layer characteristics after 25 May, while the camp was drifting over the Yermak Plateau. Prior to the 25 May, the mixed layer was deep (average of 64 m) and close to the freezing point. After the 25 May, it was very shallow (average of 6 m) and had temperatures significantly above freezing. A remnant winter mixed layer was still present below the newly formed mixed layer for some time. The shallow mixed layer coincided with the presence of a phytoplankton bloom under the snow-covered ice [*Assmy et al.*, 2017]. The vertical temperature gradient at the base of the mixed layer also showed a shift after the 25 May with a mean value prior to this date of 0.25 °C m^{-1} that dropped to 0.01 °C m^{-1} afterwards [*Meyer et al.*, 2017].

3.4. Surface and subsurface currents

Drift speed of the ice camps throughout the expedition averaged 0.17 m s^{-1} with peaks above 0.50 m s^{-1}. The overall drift direction was south-west towards Fram Strait. Stronger mean ocean currents were generally recorded at the end of each drift when the ice camp approached the sea ice edge, shallower bathymetry, and the AW inflow. Most of the observed peaks in drift speed were associated with the passage of storms. The storms also appeared to influence the observed mean absolute current speeds in the upper 23 m to 55 m. Observed absolute mean current speeds below 50 m depth varied from a minimum of 0.02 m s^{-1} with direction rotating with tides in the Nansen Basin during Floe 2, to values exceeding 0.20 m s^{-1} flowing north-east on the Svalbard continental shelf during

Floe 1. In the south-western part of the Yermak Plateau current speed was moderate with westwards and north-west direction; $0.11\,\mathrm{m\,s^{-1}}$ during Floe 3 and $0.17\,\mathrm{m\,s^{-1}}$ during Floe 4 [*Meyer et al.*, 2017].

3.5. Tides

Tidal signals were weak in the Nansen Basin during Floe 2 with both observed and predicted average current values of $0.02\,\mathrm{m\,s^{-1}}$. Tides on the Yermak Plateau and on its slopes between April and June were relatively strong and dominated the current signal, with observed current signals at tidal frequencies reaching $0.42\,\mathrm{m\,s^{-1}}$ [*Meyer et al.*, 2017].

4. Results: Mixing and heat flux estimates

The structure and magnitude of the oceanic heat fluxes throughout the N-ICE2015 campaign are sketched and quantified in Fig. 4, summarizing our main findings: Storms significantly increase heat fluxes at the ice-ocean interface; the combination of storms with presence of Atlantic Water leads to very large heat fluxes at the ice-ocean interface associated with massive basal sea ice melt events; heat fluxes are enhanced at the 0 °C isotherm and occasionally over steep topography. The contributions from different forcing conditions are presented in detail in the following subsections. The values of dissipation rate estimates over the N-ICE2015 campaign varied from intense episodic events concentrated above the pycnocline depth reaching $\mathrm{O}(10^{-5})\mathrm{W\,kg^{-1}}$ and even higher values not resolved by our instrument, to background values below the pycnocline averaging $3 \times 10^{-9}\,\mathrm{W\,kg^{-1}}$ (Fig. 2c and Table 2). Estimated heat fluxes during the N-ICE2015 campaign varied over several orders of magnitude (Fig. 5b). The overall mean value below the pycnocline was $2\,\mathrm{W\,m^{-2}}$, while mean values in the pycnocline and at the ice-ocean interface were $6\,\mathrm{W\,m^{-2}}$

and 14 W m^{-2} respectively (Fig. 4 and Table 2). Heat flux values at the ice-ocean interface were 10 times larger in the late spring after 25 May than prior to 25 May.

4.1. Wind impact

Sea ice dampens the response of the ocean to atmospheric forcing compared to open ocean conditions [*Rainville et al.*, 2011]. Nevertheless, a storm with large wind speeds taking place over Arctic sea ice will impact the drift of the ice, and therefore shear in the upper ocean layer. To quantify the impact of the wind on turbulence and heat flux during the N-ICE2015 campaign, we identified microstructure sets sampled during periods of storms only (41 sets) and key storms only (10 sets). These microstructure sets exclude periods when Atlantic Water was shallow and when topography was steep.

Storms clearly enhanced mixing in the upper ocean: Observed episodic mixing events at the ice-ocean interface and in the pycnocline appeared to match storm events and were associated with high sea ice drift speeds (Fig. 2a). Dissipation rates at the ice-ocean interface were 11 times larger during storms and 28 times larger during key storms than during periods without enhanced forcing (Fig. 6a). The impact of storms on heat flux was significant both at the ice-ocean interface and in the pycnocline layer. During key storms, heat flux increased fourfold at the ice-ocean interface and fourfold in the pycnocline layer compared to periods when there was no forcing (Fig. 6e and Table 2). No forcing means that no storms are taking place, Atlantic Water is deeper than 100 m from the pycnocline depth and there is no steep topography.

4.2. The 0 °C isotherm

Throughout the six months of observations, the 0 °C isotherm was associated with large temperature gradients that led to large positive heat fluxes: the mean heat flux within ±25 m of the 0 °C isotherm was 17 W m^{-2}, four times larger than the overall mean value. The closer to the 0 °C isotherm, the larger heat fluxes in the water column were and the less likely they were to be negative (Fig. 7).

The large heat flux values observed at the 0 °C isotherm can be explained by the fact that the 0 °C isotherm is a natural boundary between waters from the Arctic at the surface (Polar Surface Waters and warm Polar Surface Waters) and waters with Atlantic origin at intermediate depths (either Modified Atlantic Water or Atlantic Water): These two families of water masses have such distinct temperature characteristics that this boundary has large temperature gradients.

4.3. Atlantic Water impact

Several events with large heat fluxes were recorded both during winter and spring. These peaks in heat flux that exceeded 300 W m^{-2}, coincided with presence of Atlantic Water within 100 m below the sea ice (Fig. 5c). The presence of Atlantic Water (water warmer than 2 °C) in the water column did not impact turbulence rates (Fig. 6b) but strongly enhanced heat fluxes (Table 2).

Heat fluxes in the warm Polar Surface Waters (warmer than 0 °C) were on average ten times larger when Atlantic Water was present (excluding sets during storms and steep topography) than when there was no forcing (Fig. 6f). The combination of storms and presence of Atlantic Water resulted in the largest turbulent rates and heat flux values recorded during N-ICE2015 (Fig. 6d, h), driven for a major part by increased temperature

gradients in the water column. Mean dissipation rates at the ice-ocean interface then reached $6 \times 10^{-6}\,\mathrm{W\,kg^{-1}}$ and mean heat flux reached $23\,\mathrm{W\,m^{-2}}$, 11 times larger than background values. Key storms combined with Atlantic Water had an even stronger impact with heat flux 17 times larger than background values at the ice-ocean interface, averaging at $37\,\mathrm{W\,m^{-2}}$.

The heat flux peaks coincided with periods of large basal sea ice melt, as recorded with IMB buoys (Fig. 5a, black line). The two main basal melt events took place at the end of Floe 3 and 4 (early June and mid-June, highlighted in blue in Fig. 5) and were associated with a freshening of the water below the sea ice (not shown). Another melt event took place earlier in the year [*Provost et al.*, 2017; *Koenig et al.*, 2016], during a large winter storm but no concomitant microstructure data were recorded due to foul weather and sea ice conditions.

4.4. Topography impact

During the N-ICE2015 campaign, the camp drifted over steep topography five times: twice along the northern edge of the Yermak Plateau, once along its eastern edge, once along its western edge and once on the Svalbard continental slope. The camp also drifted twice over flat topography in the Nansen Basin (Fig. 1).

A total of 18 microstructure sets (56 profiles) were recorded over steep topography, of which 10 sets coincided with storms and 5 sets (21 profiles) took place when no storm or Atlantic Water were present. The steep topography sections were associated with enhanced dissipation rates (fourfold increase) at depth below 150 m (Fig. 6c and Table 2). The impact of steep topography was particularly strong on the section along the northern edge of the Plateau on 21 April 2015 with dissipation rates 15 times larger below 150 m

in three consecutive profiles (Fig. 8a). The impact of steep topography on heat flux was discernible only over the steep region sampled on 21 April with sporadic peaks in heat flux of 10 to 15 $\mathrm{W\,m^{-2}}$ in the 70-200 m depth range (Fig. 6g black line and Fig. 8b).

It is likely that the interaction of tides with the steep topography is responsible for the enhanced energy observed in the water column. Strong tidal signals have been shown previously to enhance mixing on and around the Yermak Plateau [*Padman and Dillon*, 1991; *Fer et al.*, 2010], while estimated tidal speed during N-ICE2015 reached 0.42 $\mathrm{m\,s^{-1}}$ [*Meyer et al.*, 2017]. Quantifying the role of tides in the observed mixing could be approached by a systematic analysis of internal wave signals in the data. Such analysis, however, does not belong to this study and will be undertaken as future work.

4.5. Comparison of microstructure profiler and Turbulence Instrument Cluster observations

Heat flux measurements from TIC data have a time resolution of 15 minutes. Heat flux estimates from microstructure profiler data on the other hand have a coarser, uneven time resolution (several sets a day).

There were no direct under-ice estimates of heat flux from the microstructure profiler data to compare with estimates from the TIC data; instead mean values in the pycnocline could be compared to the 1 m depth TIC data set. Microstructure mean pycnocline estimates of heat flux were similar to the TIC ice-ocean interface estimates (Fig. 5b). It is reasonable to expect a continuity of the vertical flux from the pycnocline up toward the ice, in particular under certain conditions: The closer to freezing point the near-surface waters were, the closer the under-ice TIC and pycnocline microstructure estimates were (Fig. 9b),

and vice versa; estimates differed most when surface waters departed significantly from the freezing point (more than 1 °C) (Fig. 9d).

The periods when the mixed layer was close to the freezing point were characterized by winter conditions when the sole source of heat was the ocean, supporting the relative agreement between under-ice and pycnocline fluxes. The periods when the mixed layer was warmer were mostly periods of the drift that were closer to the ice edge. Close to the ice edge, strong lateral gradients and interleaving could explain the observed differences between pycnocline and ice-ocean interface vertical heat fluxes.

5. Discussion

5.1. Sources and attribution

Mean winter (January through March) mixing and heat flux values in the Nansen Basin were the first winter measurements in this area and averaged $5 \times 10^{-9}\,\mathrm{W\,kg^{-1}}$ and $5\,\mathrm{W\,m^{-2}}$ in the pycnocline respectively. When periods with storms were excluded, these values were $3 \times 10^{-9}\,\mathrm{W\,kg^{-1}}$ and $3\,\mathrm{W\,m^{-2}}$ in the pycnocline and $2 \times 10^{-9}\,\mathrm{W\,kg^{-1}}$ and $1\,\mathrm{W\,m^{-2}}$ below the pycnocline (Table 2), which is at the noise level of the instrument (1-3 $\times 10^{-9}\,\mathrm{W\,kg^{-1}}$). Such values are similar to previous observations north of Svalbard [*Fer et al.*, 2010], or on the Chukchi borderland [*Shaw et al.*, 2009] and higher than observations from the Amundsen Basin [*Sirevaag and Fer*, 2012] or from the Beaufort Sea [*Padman and Dillon*, 1991]. Ice-ocean interface average winter dissipation rate and heat flux values were $8 \times 10^{-8}\,\mathrm{W\,kg^{-1}}$ and $2\,\mathrm{W\,m^{-2}}$ respectively. The average winter ice-ocean heat flux observed during N-ICE2015 matches the Arctic surface heat flux required to keep ice thickness at equilibrium [*Maykut and Untersteiner*, 1971].

Wind, Atlantic Water presence, and topography influenced observed mixing rates and heat flux (Fig. 6). The wind impacted dissipation rates under the ice as deep as the base of the pycnocline in winter while heat fluxes were enhanced at the ice-ocean interface and in the pycnocline layer. The presence of Atlantic Water in the water column enhanced heat flux in the warm Polar Surface Waters (above the 0 °C isotherm) by increasing the vertical temperature gradient below the mixed layer. Steep topography was associated with high dissipation rates below 150 m depth on several occasions, while enhanced heat fluxes over steep topography were only observed once on 21 April. This implies that under the right circumstances, deep topographic features such as the slope around the Yermak Plateau can enhance heat flux into the mixed layer, potentially affecting the sea ice energy budget.

Storms that occurred during the parts of the drifts over the Atlantic Water pathways led to the largest heat fluxes recorded during the N-ICE2015 campaign (Fig. 6h). This concurs with findings from the TIC data analysis [*Peterson et al.*, 2017] and from the winter ice mass balance buoys data analysis [*Provost et al.*, 2017]. When storms and Atlantic Water were combined, the contribution of wind forcing to vertical mixing could happen via increased shear between the accelerated mixed layer slab above the deeper water, leading to vertical entrainment of deeper warm waters, or increased mixing across the pycnocline through breaking of energized near-inertial internal waves [*Fer*, 2014]. This mixing combined with large temperature gradients associated with shallow Atlantic Water led to very large heat fluxes and large sea ice basal melt discussed in Section 5.3.

By integrating the observed heat fluxes in the water column, the relative role of each forcing mechanism can be quantified for the six months of the N-ICE2015 campaign: 56 %

of the total integrated heat fluxes were observed when Atlantic Water and storms only were combined. The other forcing mechanisms accounted for much less, with 14 % during storms only, and 6 % over Atlantic Water only. The integrated heat fluxes during the calm periods over the deep Nansen Basin represented 2 %. This can be partially explained by the length of time for each of these conditions during the campaign. By normalizing these percentages by the number of days, we can estimate the relative importance of each forcing condition over equal time periods relative to the calm deep Basin, which we can summarize with the following ratio:

Atlantic Water & storms, to Atlantic Water, to storms, to calm Nansen Basin = 6 : 5 : 2 : 1. When inflowing Atlantic Water is present, storms enhanced heat fluxes by a factor 6 compared with quiescent conditions over the deep Basin. Atlantic Water only and storms only enhanced heat flux by factors 5 and 2 respectively. We did not include steep topography in this analysis for several reasons: its impact was minimal in our observations, lack of data below 300 m and small sample of days for steep topography only conditions. Topography might still be important when conditions are different, for example on the continental shelf, in shallower waters than on the Yermak Plateau.

5.2. Balance between horizontal and vertical heat fluxes

Ignoring radiative flux divergence and latent heat flux from phase change, the changes in the temperature of the upper ocean layer beneath the drifting sea ice can be described by a balance between the temporal change, the vertical divergence of heat flux, and the horizontal divergence of heat flux [*McPhee*, 1992]. We define the temporal change in temperature as $\partial T/\partial t$, the vertical divergence of heat flux as $\nabla_z \mathrm{KVF}_H$ and the horizontal

divergence of heat flux as $\nabla_h \mathrm{KAF}_H$, where KVF_H is the kinematic vertical heat flux and KAF_H is the kinematic advective (or horizontal) heat flux. The simplified balance is then

$$\nabla_h \mathrm{KAF}_H = -\nabla_z \mathrm{KVF}_H - \partial T/\partial t. \tag{4}$$

Here, we use measurements between the surface and the pycnocline depth: the vertical divergence of heat flux can be estimated from the difference in heat flux measured at the ice-ocean interface and at the pycnocline depth: $\nabla_z \mathrm{KVF}_H = (F_{Htop} - F_{Hbottom})/(\rho Cp \Delta z)$, where $F_{H,top}$ is the ocean-ice interface heat flux (in $\mathrm{W\,m^{-2}}$ or $\mathrm{J\,s^{-1}\,m^{-2}}$), $F_{Hbottom}$ is the bulk heat flux in the pycnocline layer, ρ is the density of seawater set at $1027\,\mathrm{kg\,m^{-3}}$, C_p is the heat capacity of seawater set at $3991.9\,\mathrm{J\,kg^{-1}\,K^{-1}}$, and Δz (m) is the water column thickness between the ice-ocean interface and the pycnocline layer. The observed temporal change in temperature ($\partial T/\partial t$) can be estimated as the change in temperature in the layer from ice-ocean interface to pycnocline depth from one microstructure set to the next one. With both $\nabla_z \mathrm{KVF}_H$ and $\partial T/\partial t$ in $\mathrm{C\ s^{-1}}$, $\nabla_h \mathrm{KAF}_H$ also has units of $\mathrm{C\ s^{-1}}$.

While changes in temperature between the surface and the pycnocline depth were mostly dominated by horizontal advection during N-ICE2015, the vertical divergence of heat flux buffered the impact of horizontal advection in June: Divergence in temperature was minimal in the winter months (January to March), with the exception of a warming event (0.3 °C) between the 6 and 16 February when Floe 1 drifted over warm Atlantic Water and a cooling event (0.1 °C) around 9 March during Floe 2. Both events were accounted for by horizontal advection. Horizontal advection also seem to dominate temperature changes in the early spring (April-May): the divergence was small for most of Floe 3 (±0.2 °C) until the 4 June when the upper water column suddenly warmed up by 2.5 °C. The upper

water column also warmed up significantly during Floe 4, 1.5 °C in June, but the large horizontal divergence term with a warming effect was partly compensated by significant vertical divergence (Fig. 10).

These observations suggest that when close to the ice edge and when the Atlantic Water was shallow near slopes, the increase in temperature divergence was driven by increased horizontal advective contributions. These warm horizontal advection events were likely partly from the warm Atlantic Water inflow (in winter and spring), and from lateral advection of solar heated water from nearby open waters (in spring only). All three main events of horizontal divergence (February, early June and mid June) took place while in areas with strong tides, during storms, and in areas nearby or over warm Atlantic Water. It is therefore difficult to identify the cause of these horizontal advection events, which could be wind driven, tidally driven, as well as linked to mesoscale structures.

5.3. Heat flux impact on the ice

The largest heat flux estimates during N-ICE2015 were recorded when the proximity to Atlantic Water was combined with storms. This happened three times: on 16 February, 2 - 5 June, and 11 - 13 June 2015. During each of these events, a storm took place, ice drift speeds were larger than $0.4\,\mathrm{m\,s^{-1}}$, and Atlantic Water was present at less than 100 m depth. Heat fluxes at the ice-ocean interface averaged $106\,\mathrm{W\,m^{-2}}$ during the last event in June. These enhanced heat fluxes lead to the warming of the water below the sea ice, which in turn triggered large basal sea ice melt. A basal melt of 25 cm per day was recorded from 5 June at the end of Floe 3, and again during Floe 4 after 10 June 2015 [A. Rösel, personal communication, September 2016 and *Rösel et al.* [2016]]. Ice mass balance buoys also observed rapid sea ice melt during the February event and derived

conductive heat fluxes estimates that peaked at $400\,\mathrm{W\,m^{-2}}$ [*Provost et al.*, 2017]. These extremely large basal melt events led to the decay of the ice, making it more vulnerable to swell and waves, and ultimately to break up events.

5.4. Conclusions

Six months of microstructure observations from the N-ICE2015 campaign allowed quantification of the impact of several environmental forcing factors on heat flux in the upper Arctic Ocean (Fig. 4). This data set is particularly valuable as it brings light to winter conditions in the Eurasian Basin, where direct observations of microstructure have not been reported before. Mean winter (January through March) pycnocline ocean heat fluxes were $3\,\mathrm{W\,m^{-2}}$ in the Nansen Basin and remained positive between storm events. Large observed variability in heat fluxes was attributed to different forcing mechanisms. Steep topography consistently enhanced dissipation rates by a factor four and in one case also increased heat fluxes at depth. The combination of storms and shallow Atlantic Water both in winter and summer induced large ocean heat flux of order $100\,\mathrm{W\,m^{-2}}$ in the upper ocean associated with massive basal sea ice melt events. This highlights the importance of predicted increased storm frequency in the Arctic that could erode local stratification and tap into warm sub-surface Atlantic Water. In winter, this would lead to reduced growth, weakening, and even melting of the sea ice, while in spring such events would accelerate the melting and break up of the sea ice. The warming and shoaling of the Atlantic Water inflow north of Svalbard and in the Barents Sea combined with increased storm frequency could lead to a significant reduction in sea ice cover further along the Atlantic Water inflow.

Acknowledgments. This work has been supported by the Norwegian Polar Institutes Centre for Ice, Climate and Ecosystems (ICE) through the N-ICE project. Additional support was obtained from the Centre for Climate Dynamics at the Bjerknes Centre through grant BASIC: Boundary Layers in the Arctic Atmosphere, Seas and Ice Dynamics. AKP is supported by the Research Council of Norway, through the project 229786. We thank N-ICE2015 participants, the captains, crews and N-ICE2015 scientists for their help in making this study possible. We also thank two anonymous reviewers for valuable comments that greatly improved the submitted manuscript. Data used in this study are publicly available at the Norwegian Polar Data Centre: https://data.npolar.no/ under the keyword N-ICE2015.

References

Aagaard, K., A. Foldvik, and S. R. Hillman (1987), The West Spitsbergen Current: Disposition and water mass transformation, *Journal of Geophysical Research: Oceans*, *92*(C4), 3778–3784.

Assmy, P., M. Fernandez-Mendez, P. Duarte, A. Meyer, A. Randelhoff, C. J. Mundy, L. M. Olsen, H. Kauko, and E. Al (2017), Leads in the Arctic pack ice enable early phytoplankton blooms below snow-covered sea ice, *Scientific Reports*, *7*(40850), doi: 10.1038/srep40850.

Carmack, E. C., I. V. Polyakov, L. Padman, I. Fer, E. Hunke, J. Hutchings, J. Jackson, D. Kelley, R. Kwok, C. Layton, H. Melling, D. Perovich, O. Persson, B. Ruddick, M.-L. Timmermans, J. M. Toole, T. Ross, S. Vavrus, and P. Winsor (2015), Towards Quantifying the Increasing Role of Oceanic Heat in Sea Ice Loss in the New Arctic,

Bulletin of the American Meteorological Society, (December), doi:10.1175/BAMS-D-13-00177.1.

Cohen, L., S. R. Hudson, V. P. Walden, R. M. Graham, and M. A. Granskog (), Meteorological conditions in a thinner Arctic sea ice regime from winter through spring during the Norwegian young sea ICE expedition (N-ICE2015), *Journal of Geophysical Research*, *Submitted*.

Dewey, R. K., R. Muench, and J. Gunn (1999), Mixing and vertical heat flux estimates in the Arctic Eurasian Basin, in *Journal of Marine Systems*, vol. 21, pp. 199–205.

Fer, I. (2006), Scaling turbulent dissipation in an Arctic fjord, in *Deep-Sea Research Part II: Topical Studies in Oceanography*, vol. 53, pp. 77–95.

Fer, I. (2009), Weak Vertical Diffusion Allows Maintenance of Cold Halocline in the Central Arctic, *Atmospheric and Oceanic Science Letters*, *2*(3), 148–152.

Fer, I. (2014), Near-Inertial Mixing in the Central Arctic Ocean, *Journal of Physical Oceanography*, *44*(8), 2031–2049, doi:10.1175/JPO-D-13-0133.1.

Fer, I., R. Skogseth, and F. Geyer (2010), Internal Waves and Mixing in the Marginal Ice Zone near the Yermak Plateau, *Journal of Physical Oceanography*, *40*(7), 1613–1630, doi:10.1175/2010JPO4371.1.

Fer, I., M. Müller, and A. K. Peterson (2015), Tidal forcing, energetics, and mixing near the Yermak Plateau, *Ocean Science*, *11*, 287–304, doi:10.5194/os-11-287-2015.

Fer, I., A. K. Peterson, A. Randelhoff, and A. Meyer (2017), One-dimensional evolution of the upper water column in the Atlantic sector of the Arctic Ocean in winter, *Journal of Geophysical Research Oceans*, *in press*, doi:10.1002/2016JC012431.

Granskog, M. A., P. Assmy, S. Gerland, G. Spreen, H. Steen, and L. H. Smedsrud (2016), Arctic research on thin ice: Understanding the consequences of ongoing Arctic sea ice loss (N-ICE2015), *Eos, Transactions American Geophysical Union*, *97*, 22–26, doi: 10.1029/2016EO044097.

Guthrie, J. D., J. H. Morison, and I. Fer (2013), Revisiting internal waves and mixing in the Arctic Ocean, *Journal of Geophysical Research: Oceans*, *118*(8), 3966–3977.

Intergovernmental Oceanographic Commission (2010), *IOC, SCOR and IAPSO, 2010: The international thermodynamic equation of seawater - 2010: Calculation and use of thermodynamic properties*, manuals an ed., 196 pp., UNESCO.

Itkin, P., G. Spreen, B. Cheng, M. Doble, F. Girard-Ardhuin, J. Haapala, S. R. Hudson, N. Hughes, L. Kaleschke, M. Nicolaus, and J. Wilkinson (), Thin ice and storms: a case study of sea ice deformation from buoy arrays deployed during N-ICE2015, *J. Geophys. Res.*, *Submitted*.

Itkin, P., G. Spreen, S. R. Hudson, M. A. Granskog, S. Gerland, A. K. Pavlov, B. Cheng, J. Haapala, M. Doble, M. Nicolaus, L. Kaleschke, J. Wilkinson, and H. Steen (2015), N-ICE2015 buoy data [Data set], *Tech. rep.*, Norwegian polar Institute, doi: 10.21334/npolar.2015.6ed9a8ca.

Jakobsson, M., L. Mayer, B. Coakley, J. A. Dowdeswell, S. Forbes, B. Fridman, H. Hodnesdal, R. Noormets, R. Pedersen, M. Rebesco, H. W. Schenke, Y. Zarayskaya, D. Accettella, A. Armstrong, R. M. Anderson, P. Bienhoff, A. Camerlenghi, I. Church, M. Edwards, J. V. Gardner, J. K. Hall, B. Hell, O. Hestvik, Y. Kristoffersen, C. Marcussen, R. Mohammad, D. Mosher, S. V. Nghiem, M. T. Pedrosa, P. G. Travaglini, and P. Weatherall (2012), The International Bathymetric Chart of the Arctic Ocean

(IBCAO) Version 3.0, *Geophysical Research Letters*, *39*(12).

Koenig, Z., C. Provost, N. Villacieros-Robineau, N. Sennéchael, and A. Meyer (2016), Winter ocean-ice interactions under thin sea ice observed by IAOOS platforms during N-ICE2015: salty surface mixed layer and active basal melt, *J. Geophys. Res.*, *121*, 7898–7916, doi:10.1002/2016JC012195.

Krishfield, R. A., and D. K. Perovich (2005), Spatial and temporal variability of oceanic heat flux to the Arctic ice pack, *Journal of Geophysical Research C: Oceans*, *110*(7), 1–20.

Lenn, Y. D., P. J. Wiles, S. Torres-Valdes, E. P. Abrahamsen, T. P. Rippeth, J. H. Simpson, S. Bacon, S. W. Laxon, I. Polyakov, V. Ivanov, and S. Kirillov (2009), Vertical mixing at intermediate depths in the Arctic boundary current, *Geophysical Research Letters*, *36*(5).

Maykut, G. a., and M. G. McPhee (1995), Solar heating of the Arctic mixed layer, *Journal of Geophysical Research*, *100*(C12), 24,691.

Maykut, G. A., and N. Untersteiner (1971), Some results from a time-dependent thermodynamic model of sea ice, *Journal of Geophysical Research*, *76*(6), 1550–1575, doi: 10.1029/JC076i006p01550.

McDougall, T. J., D. R. Jackett, F. J. Millero, R. Pawlowicz, and P. M. Barker (2012), A global algorithm for estimating Absolute Salinity, *Ocean Science*, *8*(6), 1123–1134.

McPhee, M. G. (1992), Turbulent heat flux in the upper ocean under sea ice, *Journal of Geophysical Research*, *97*(C4), 5365, doi:10.1029/92JC00239.

Meyer, A., B. M. Sloyan, K. L. Polzin, H. E. Phillips, and N. L. Bindoff (2015), Mixing variability in the Southern Ocean, *Journal of Physical Oceanography*, *45*, 966–987, doi:

10.1175/JPO-D-14-0110.1.

Meyer, A., A. Sundfjord, I. Fer, C. Provost, N. Villacieros-Robineau, Z. Koenig, I. H. Onarheim, L. H. Smedsrud, P. Duarte, P. Dodd, R. M. Graham, and H. Kauko (2017), Winter to summer hydrographic and current observations in the Arctic Ocean north of Svalbard, *Journal of Geophysical Research*, *In press*, doi:10.1002/2016JC012391.

Morison, J. H., C. E. Long, and M. D. Levine (1985), Internal wave dissipation under sea ice, *Journal of Geophysical Research*, *90*(C6), 11,959, doi:10.1029/JC090iC06p11959.

Osborn, T. R. (1980), Estimates of the local-rate of vertical diffusion from dissipation measurements, *Journal of Physical Oceanography*, *10*(1), 83–89.

Padman, L., and T. M. Dillon (1991), Turbulent mixing near the Yermak Plateau during the Coordinated Eastern Arctic Experiment, *Journal of Geophysical Research*, *96*(C3), 4769, doi:10.1029/90JC02260.

Peralta-Ferriz, C., and R. A. Woodgate (2015), Seasonal and interannual variability of pan-Arctic surface mixed layer properties from 1979 to 2012 from hydrographic data, and the dominance of stratification for multiyear mixed layer depth shoaling, *Progress in Oceanography*, *134*, 19–53, doi:10.1016/j.pocean.2014.12.005.

Peterson, A. K., I. Fer, M. G. McPhee, and A. Randelhoff (2017), Turbulent Heat and Momentum Fluxes in the Upper Ocean Under Arctic Sea Ice, *J. Geophys. Res.*, *In press*, doi:10.1002/2016JC012283.

Pinkel, R. (2005), Near-Inertial Wave Propagation in the Western Arctic, *Journal of Physical Oceanography*, *35*(5), 645–665.

Polyakov, I. V., A. V. Pnyushkov, R. Rember, L. Padman, E. C. Carmack, and J. M. Jackson (2013), Winter Convection Transports Atlantic Water Heat to the Surface Layer

in the Eastern Arctic Ocean*, *Journal of Physical Oceanography*, *43*(1981), 2142–2155, doi:10.1175/JPO-D-12-0169.1.

Prandke, H., and A. Stips (1998), Test measurements with an operational microstructure-turbulence profiler: Detection limit of dissipation rates, *Aquatic Sciences*, *60*(3), 191–209, doi:10.1007/s000270050036.

Provost, C., N. Sennéchael, J. Miguet, P. Itkin, A. Rösel, Z. Koenig, N. Villacieros-Robineau, and M. A. Granskog (2017), Observations of snow-ice formation in a thinner Arctic sea ice regime during the N-ICE2015 campaign: influence of basal ice melt and storms, *Journal of Geophysical Research*, *In press*, doi:10.1002/2016JC012011.

Rainville, L., and P. Winsor (2008), Mixing across the Arctic Ocean: Microstructure observations during the Beringia 2005 Expedition, *Geophysical Research Letters*, *35*(8).

Rainville, L., C. Lee, and R. Woodgate (2011), Impact of Wind-Driven Mixing in the Arctic Ocean, *Oceanography*, *24*(3), 136–145.

Renner, A. H. H., S. Gerland, C. Haas, G. Spreen, J. F. Beckers, E. Hansen, M. Nicolaus, and H. Goodwin (2014), Evidence of Arctic sea ice thinning from direct observations, *Geophysical Research Letters*, *41*(14), 5029–5036.

Rippeth, T. P., B. J. Lincoln, Y.-d. Lenn, J. A. M. Green, A. Sundfjord, and S. Bacon (2015), Tide-mediated warming of Arctic halocline by Atlantic heat fluxes over rough topography, *Nature Geoscience*, *8*(3), 191–194, doi:10.1038/ngeo2350.

Rösel, A., D. V. Divine, J. A. King, M. Nicolaus, G. Spreen, P. Itkin, C. M. Polashenski, ..., and M. A. Granskog (2016), N-ICE2015 total (snow and ice) thickness data from EM31 [Data set], *Tech. rep.*, Norwegian Polar Institute, doi:10.21334/npolar.2016.70352512.

Rudels, B., R. Meyer, E. Fahrbach, V. V. Ivanov, S. Østerhus, D. Quadfasel, U. Schauer, V. Tverberg, and R. a. Woodgate (2000), Water mass distribution in Fram Strait and over the Yermak Plateau in summer 1997, *Annales Geophysicae*, *18*(6), 0687–0705, doi:10.1007/s005850000216.

Shaw, W. J., and T. P. Stanton (2014), Vertical diffusivity of the Western Arctic Ocean halocline, *Journal of Geophysical Research: Oceans*, *119*(8), 5017–5038, doi: 10.1002/2013JC009598.

Shaw, W. J., I. Fer, M. G. McPhee, J. H. Morison, and D. G. Martinson (2009), Role of the upper ocean in the energy budget of Arctic sea ice during SHEBA, *Journal of Geophysical Research*, *114*(C06012).

Sirevaag, A., and I. Fer (2009), Early Spring Oceanic Heat Fluxes and Mixing Observed from Drift Stations North of Svalbard*, *Journal of Physical Oceanography*, *39*(12), 3049–3069, doi:10.1175/2009JPO4172.1.

Sirevaag, A., and I. Fer (2012), Vertical heat transfer in the Arctic Ocean: The role of double-diffusive mixing, *Journal of Geophysical Research: Oceans*, *117*(7).

Steele, M., and J. H. Morison (1993), Hydrography and vertical fluxes of heat and salt northeast of Svalbard in autumn, *Journal of Geophysical Research*, *98*(C6), 10,013.

Untersteiner, N. (1988), On the ice and heat balance in Fram Strait, *J. Geophys. Res.*, *93*(7), 527–531.

Yamazaki, H., and R. G. Lueck (1990), Why Oceanic Dissipation Rates Are Not Lognormal, *Journal of Physical Oceanography*, *20*(1907-1918).

Table 1. N-ICE2015 campaign overview with key variables (see Section 2.7. for details) averaged over each drift floe.

Drift floe	**Floe 1**	**Floe 2**	**Floe 3**	**Floe 4**
Season	Winter	Winter	Spring	Spring
Start date	15 Jan 2015	24 Feb 2015	18 Apr 2015	7 Jun 2015
Start position	83.2^o N 21.6^o E	83° N 27.4^o E	83.2^o N 13.5^o E	81.1^o N 14.4^o E
End date	21 Feb 2015	19 Mar 2015	5 Jun 2015	22 Jun 2015
End position	81.2^oN 20.3^oE	82.5^oN 22.6^oE	79.9^oN 3.1^oE	80.1^oN 5.7^oE
Duration (days)	38	24	49	16
Drift speed	0.16 ms^{-1}	0.21 ms^{-1}	0.14 ms^{-1}	0.21 ms^{-1}
Distance to open water	137 km	239 km	120 km	43 km
Ocean bottom depth	3485 m	3990 m	1482 m	1176 m
Mixed layer depth	57.0 m	83.7 m	47.8 m	4.6 m
Air temperature	-27.4^oC	-13.7^oC	-10.1^oC	-0.4^oC
Number of MSS profiles (sets)	71 (21)	55 (25)	333 (97)	129 (30)
Hours of collected TIC data	524	155	892	200

Table 2. Average oceanic and turbulent parameters in various layers and under different forcing (see Section 2.7. for details) for the N-ICE2015 campaign: Conservative Temperature Θ (^{o}C), Absolute Salinity S_A ($g\,kg^{-1}$), buoyancy frequency squared N^2 ($(rad\,s^{-1})^2$), dissipation rate ($W\,kg^{-1}$), and heat flux ($W\,m^{-2}$).

	Θ	S_A	**Stratification** N^2	**Dissipation** ϵ	**Heat flux**
	°C	$\mathrm{g\,kg^{-1}}$	$(\mathrm{rad\,s^{-1}})^2$	$\mathrm{W\,kg^{-1}}$	$\mathrm{W\,m^{-2}}$
N-ICE2015 1 m (TIC data)	-1.8	34.1	(-)	4×10^{-7}	14
N-ICE2015 pycnocline	-0.9	34.4	1×10^{-4}	6×10^{-8}	6
N-ICE2015 below pycnocline	1.7	35.0	1×10^{-5}	3×10^{-9}	2
In pycnocline when no forcing	-1.2	34.5	5×10^{-5}	4×10^{-9}	4
In pycnocline when storms only	-1.0	34.6	5×10^{-5}	7×10^{-9}	6
In pycnocline when key storms only	-1.1	34.6	5×10^{-5}	1×10^{-8}	12
In pycnocline when Atlantic Water present only	-0.8	33.6	5×10^{-4}	4×10^{-8}	5
In pycnocline when storms and AW present	-0.6	34.3	3×10^{-4}	1×10^{-7}	8
In pycnocline during basal ice melt	0.0	34.0	5×10^{-4}	2×10^{-7}	16
Below pycnocline when flat topography only	1.3	35.0	1×10^{-5}	2×10^{-9}	1
Below pycnocline when steep topography only	0.6	34.8	2×10^{-5}	7×10^{-9}	5
Below pycnocline in quiescent Nansen Basin	1.3	35.0	1×10^{-5}	2×10^{-9}	1

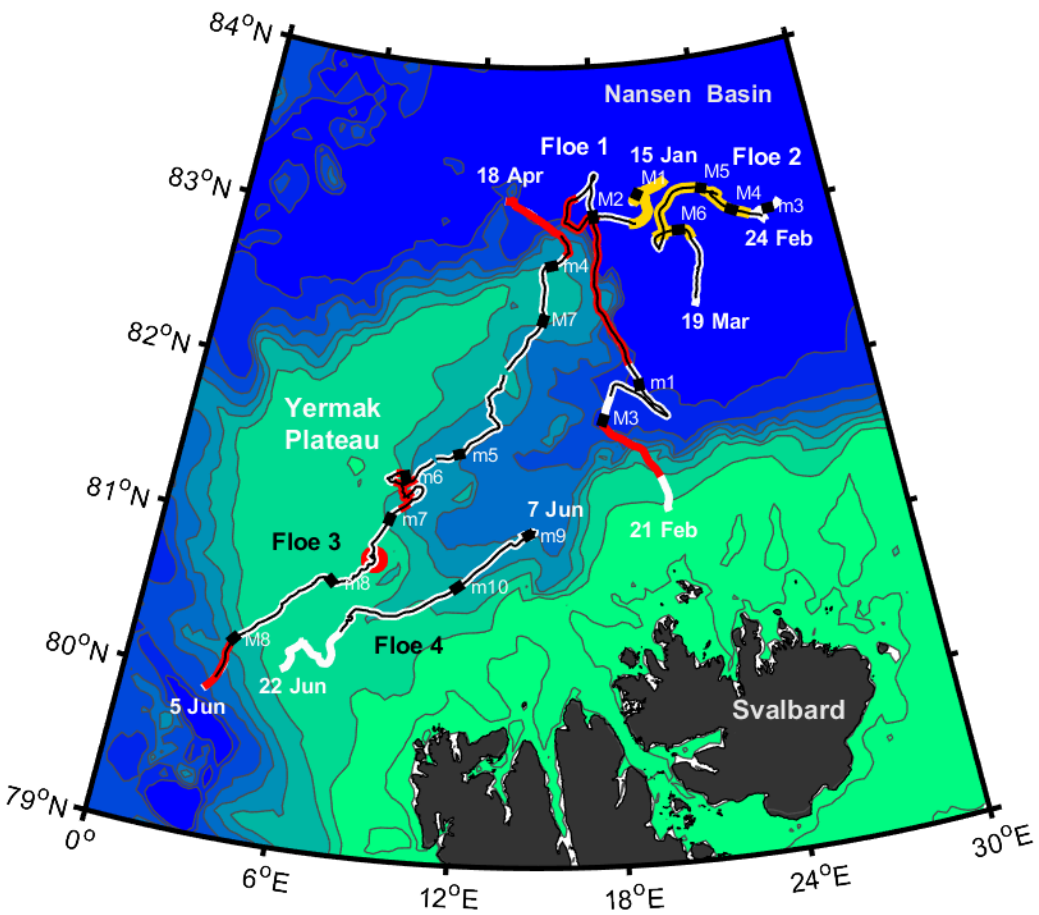

Figure 1. Trajectories of the four N-ICE2015 ice drifts between 15 January and 22 June 2015 with underlying topographic contours (100, 500, 1000, 1500, 2000, 2500, 3000, and 3500 m). Sections of the drifts over steep topography are highlighted in red, while sections over flat topography are highlighted in yellow following definitions in Section 2.7.2.. Storms described in *Cohen et al.* are shown as black rectangles and their names indicated. Periods during which microstructure profiler data were collected are indicated by thin black line along drift track. Large red dot corresponds to 25 May 2015.

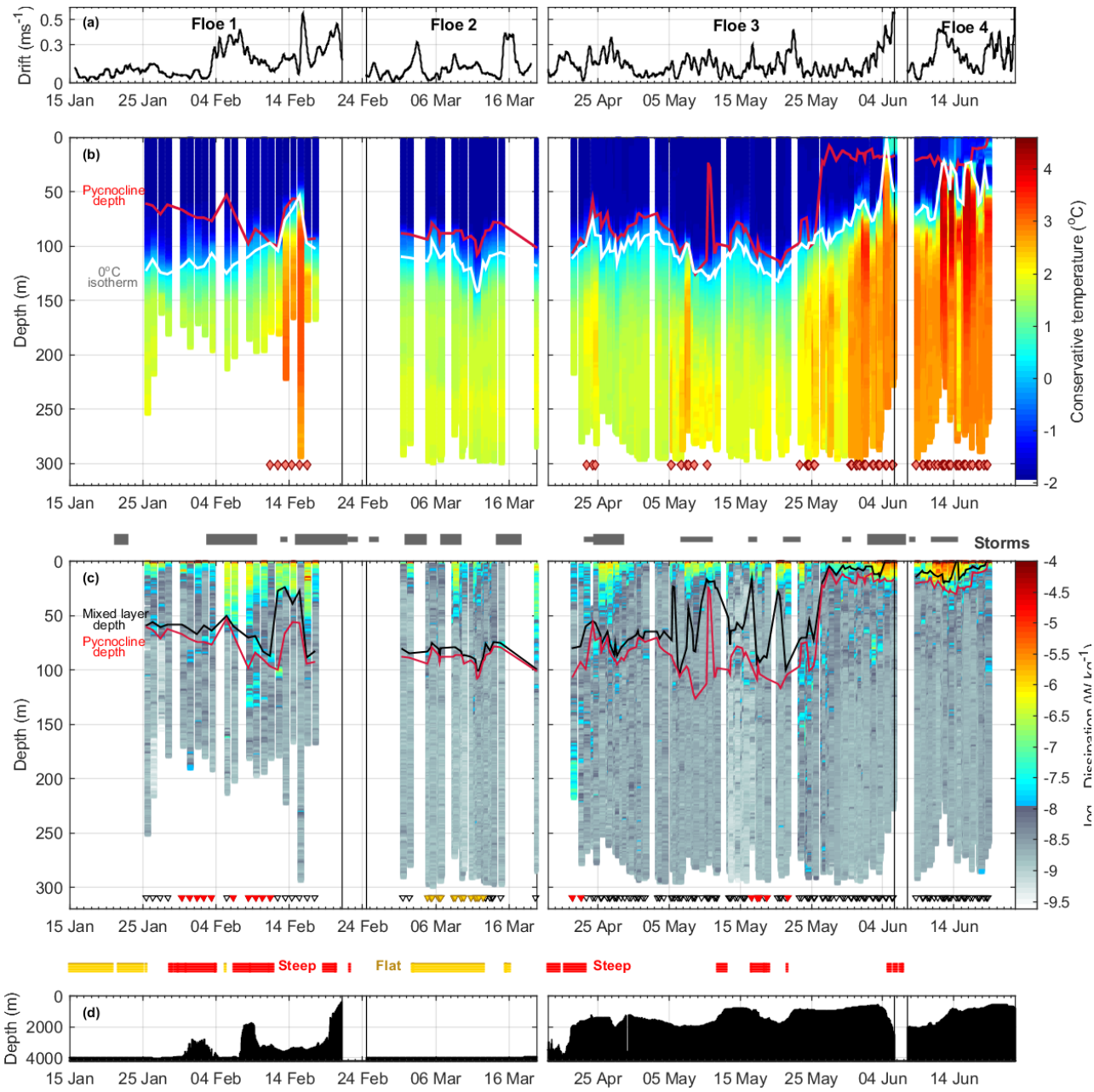

Figure 2. Overview of the four N-ICE2015 drifts, with time series of (a) sea ice drift speed during the N-ICE2015 campaign; (b) Vertical distribution of conservative temperature in the upper 300 m along the drift trajectories. The red line shows the pycnocline depth while the white line shows the depth of the 0 °C isotherm. Red diamonds indicate sets in which Atlantic Water was present; (c) Vertical distribution of dissipation rate in the upper 300 m along the drift trajectories. The black line shows the mixed layer depth while the red line shows the pycnocline depth. The time of each MSS set is marked by small triangles: red triangles indicate sets above steep topography while yellow triangles are sets above flat topography; (d) Seafloor depth along the drift tracks. Grey blocks indicate major storms (thicker boxes) and minor storms (thinner boxes) [*Cohen et al.*]. Red blocks indicate steep topography and yellow block flat topography along the drift tracks.

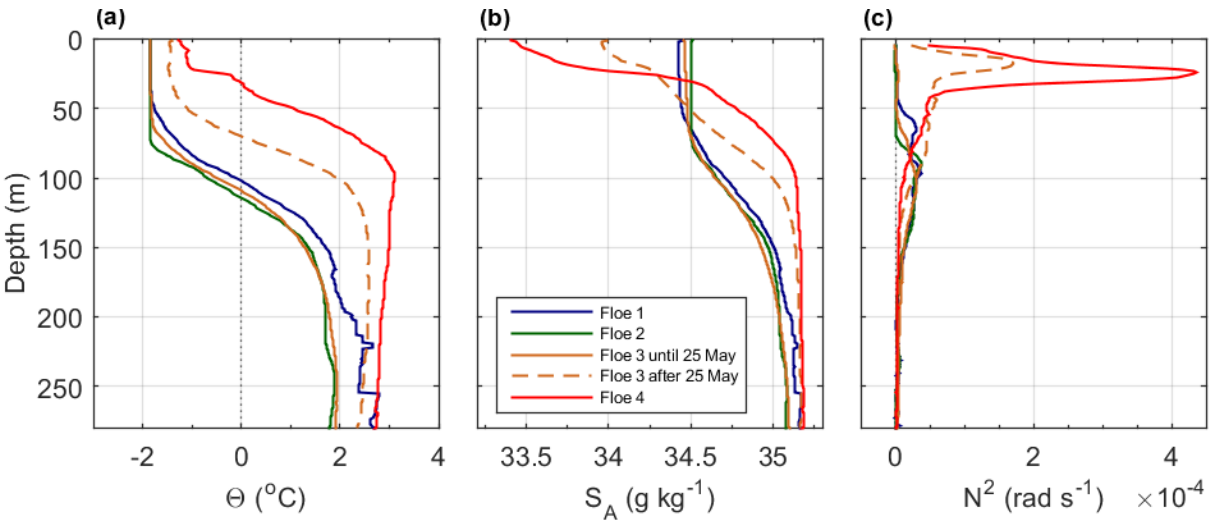

Figure 3. Mean vertical profiles of (a) Conservative Temperature, (b) Absolute Salinity, and (c) buoyancy frequency squared as function of depth during Floe 1 (blue), Floe 2 (green), Floe 3 before 25 May (yellow), Floe 3 after 25 May (dashed yellow) and Floe 4 (red).

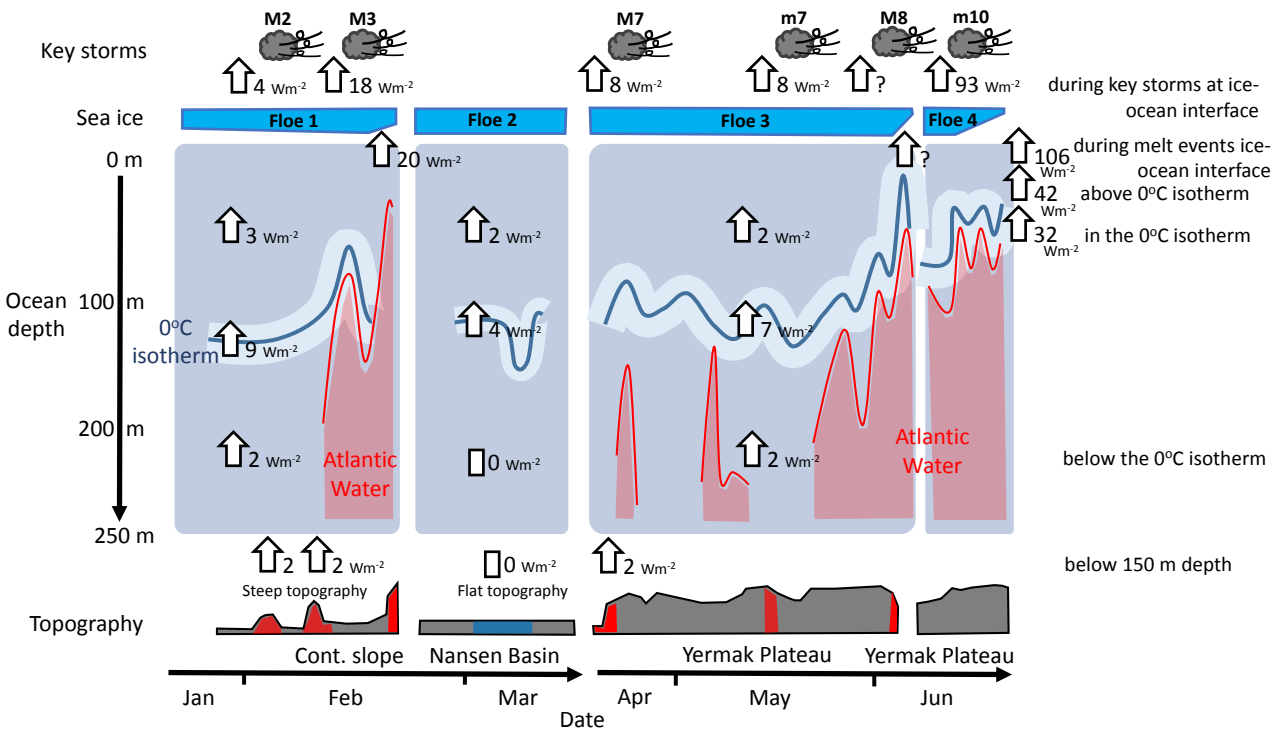

Figure 4. Schematic of ocean heat flux estimates on various time and spatial scales during the N-ICE2015 campaign. Clouds indicate key storms and associated mean heat flux at the ice-ocean interface (1 m depth from TIC data). The thinning of blue blocks indicate large basal ice melt events and associated mean heat flux in the ice-ocean interface are shown. In the ocean, the blue line shows the 0 °C isotherm depth and associated mean heat flux within a 50 m window centred on it. Mean heat flux (from MSS data) above and below the 0 °C isotherm layer are indicated for each floe. Vertical distribution of Atlantic Water is indicated by red shading. Topography is shown in gray with steep regions highlighted in red and flat regions in blue; associated mean heat flux below 150 m depth for steep and flat sections are indicated. Question marks indicate events during which heat flux estimates are not available.

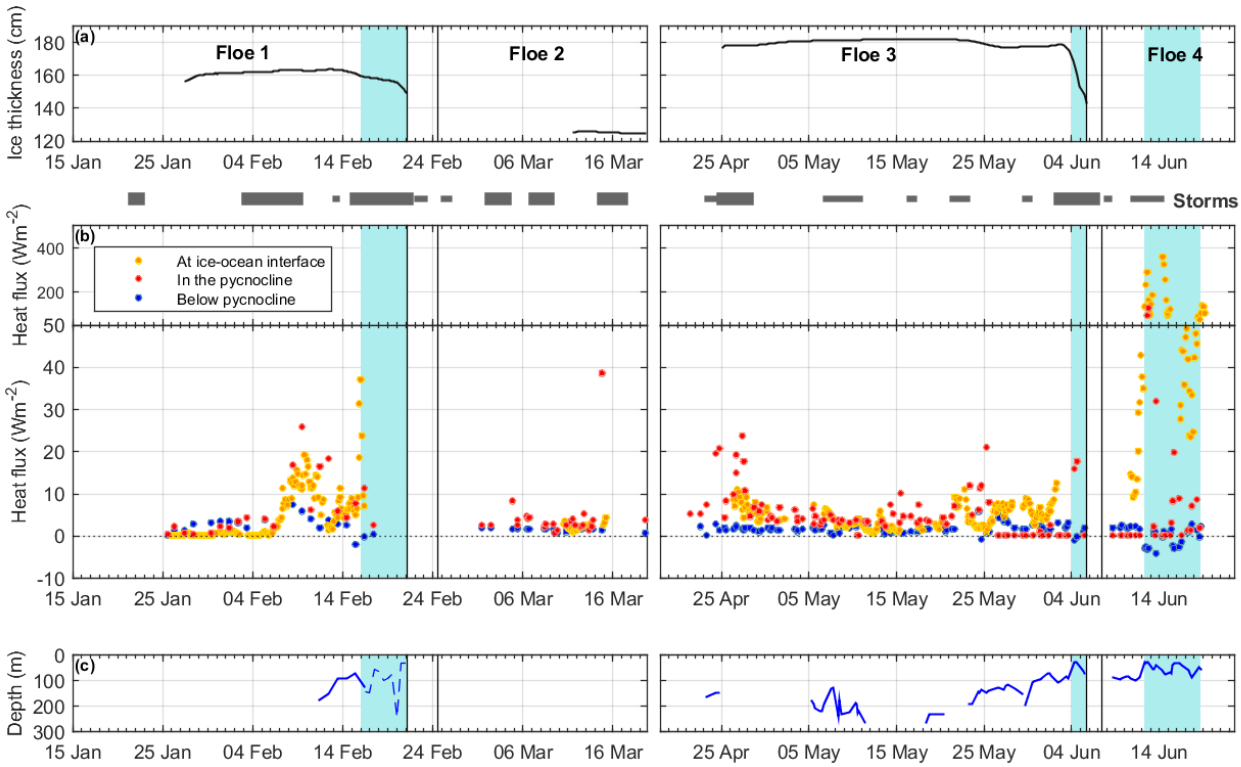

Figure 5. Overview of the four N-ICE2015 drifts, with time series of (a) sea ice thickness estimates for Floe 1, 2 and 3 from ice mass balance buoys SIMBA 2015h, SIMBA 2015d, and SIMBA 2015c respectively [*Provost et al.*, 2017; *Itkin et al.*, 2015]; (b) Mean heat flux time series along the drift trajectories at the ice ocean interface (1 m below the ice; yellow), in the pycnocline (red), and below the pycnocline (blue); (c) Depth of the upper boundary of Atlantic Water when present from microstructure profiler data (solid line) and from ship CTD data (dashed line). Grey blocks indicate major storms (thicker boxes) and minor storms (thinner boxes) [*Cohen et al.*]. Periods of large basal ice melt events are highlighted in blue shading across the plots [*Rösel et al.*, 2016].

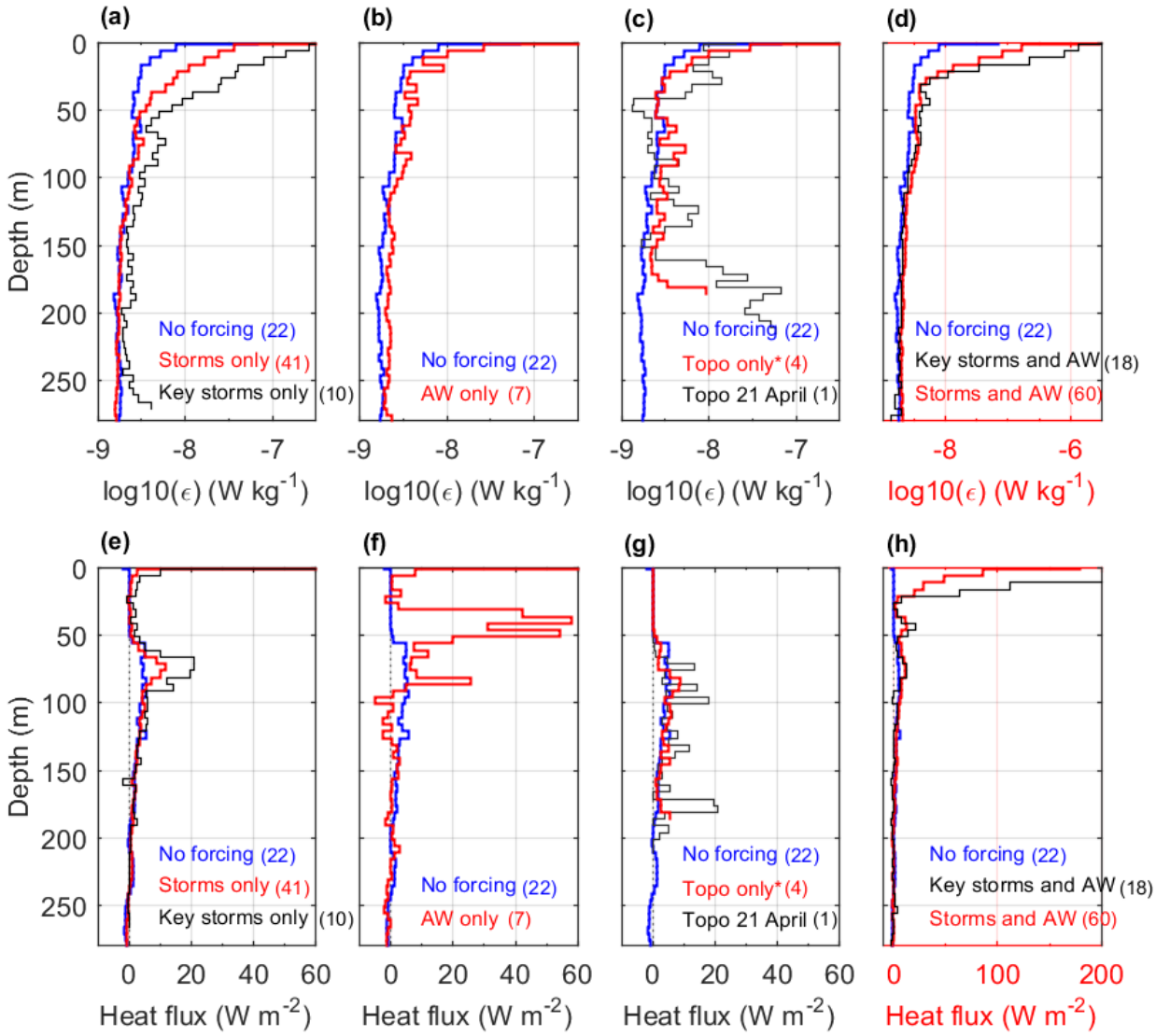

Figure 6. Mean vertical profiles of (top) dissipation rate from microstructure profiler data and (bottom) heat flux for the whole of N-ICE2015 campaign, subsampled for 'no forcing' conditions (blue, all panels), and for sets affected by (a and e) storms and key storms, (b and f) shallow Atlantic Water, (c and g) steep topography only (excluding 21 April) and 21 April only, (d and h) storms and Atlantic Water and key storms and Atlantic Water. No forcing means no storms, no shallow Atlantic Water and no steep topography. Sets of profiles used to make the mean profile for a given forcing exclude sets when other forcing is present. The numbers of sets of profiles used to make the mean profiles are given in brackets. Note the different x-axis scale for subplots (d) and (h).

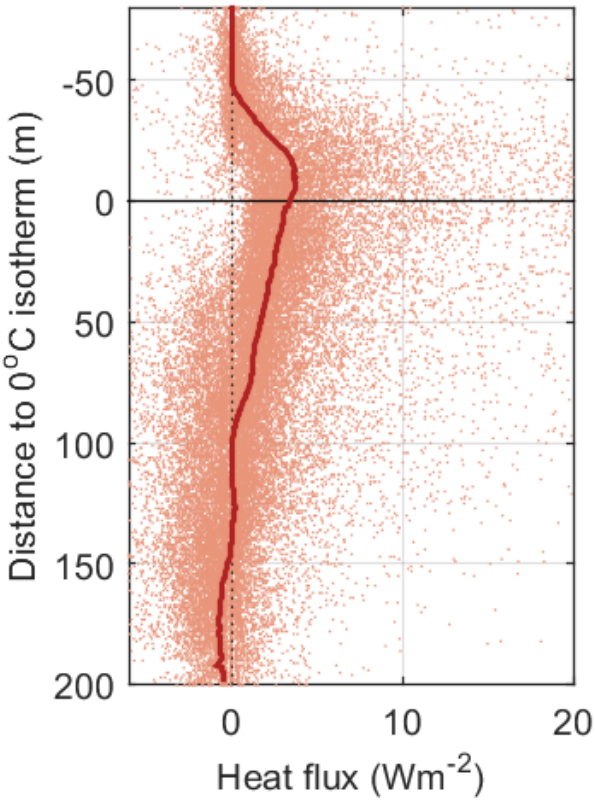

Figure 7. Median vertical profile of heat flux as a function of distance to the 0 °C isotherm, where −50 m indicates data in the water column 50 m above the 0 °C isotherm and 100 m indicates data 100 m below the 0 °C isotherm. All data used to derive the median profile are shown as individual points.

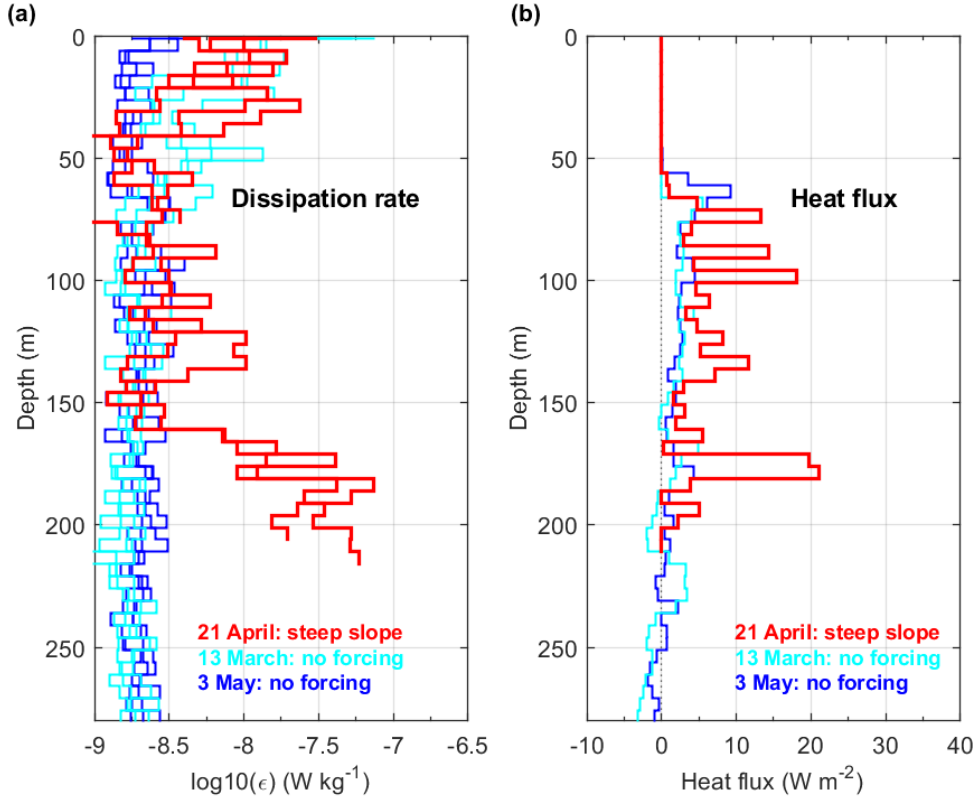

Figure 8. (a) The three vertical individual profiles of dissipation rate that when averaged constitute the microstructure set from 21 April over steep topography (red), from a nearby set with no forcing (3 May, dark blue), and from a quiet winter set with no forcing (13 March, cyan). (b) Resulting vertical heat flux profiles for the dissipation rate profiles in (a) over steep topography (red), when there is no forcing in spring (dark blue) and in winter (cyan). No forcing means no storms, no shallow Atlantic Water and no steep topography.

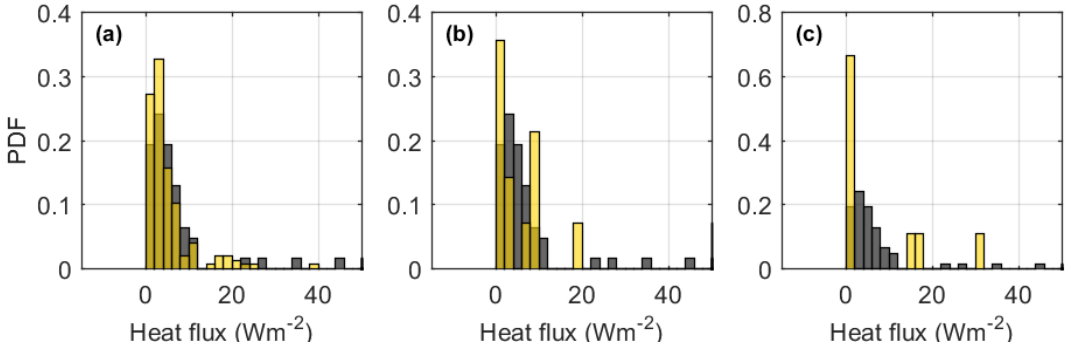

Figure 9. Histograms of the heat flux estimates from the TIC data at 1 m depth (gray) and pycnocline heat flux estimates from microstructure profiler data (yellow) for profiles with a departure from freezing point in the upper 5 m that is (a) small, less than 0.2 °C, (b) moderate, 0.2-1 °C, and (c) large, more than 1 °C.

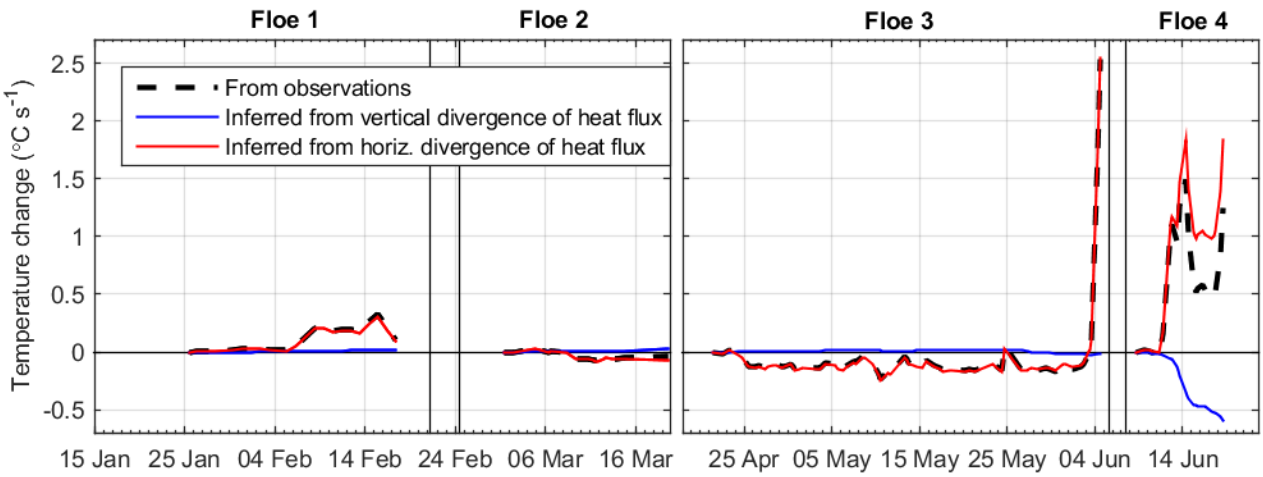

Figure 10. Time series of the change in temperature with time (°C s^{-1}) of the observed mean temperature in the layer between the ice-ocean interface and the pycnocline depth (dashed black line), the temperature change inferred from the vertical divergence of measured heat flux (blue line), and the temperature change estimated from horizontal divergence of measured heat flux (red line).